LAWRENCE
LIVERMORE
NATIONAL
LABORATORY

LLNL-JRNL-646673

FROM ELECTRONIC STRUCTURE TO THERMODYNAMICS OF ACTINIDE-BASED ALLOYS

P. E. A. Turchi, P. Soderlind, A. I. Landa

November 21, 2013

The Journal of The Minerals, Metals and Materials Society (TMS)

Disclaimer

FROM ELECTRONIC STRUCTURE TO THERMODYNAMICS OF ACTINIDE-BASED ALLOYS

P. E. A. TURCHI[1,2], P. SÖDERLIND[1], AND A. I. LANDA[1]

1.–Lawrence Livermore National Laboratory, Physical and Life Sciences Directorate, P. O. Box Livermore, CA 94551,USA. 2.–e-mail: Turchi1@llnl.gov

Abstract: In this brief review we show that thermodynamic modeling of complex multi-component actinide-based alloys is crucial for fuel development and for predicting the impact of evolving fuel chemistry with time on materials performance. With input from energetics and equilibrium properties of alloys from *ab initio* electronic-structure calculations, within the framework of density-functional theory, the CALPHAD methodology is a viable approach to thermodynamic assessment for this class of materials. Despite the limited availability of experimental thermodynamic data, this approach can predict important features in the phase diagram and, perhaps more importantly, guide and motivate further experiments for validating the methodology and the data for subsequent modeling of materials performance on a higher level.

Keywords: nuclear reactor materials, first-principles, actinide, thermodynamics, phase diagram

INTRODUCTION

The development of sustainable nuclear energy is critical to the energy security of the United States. Today only a small fraction of the enriched uranium that is used to fuel the U.S. fleet of ~104 civilian reactors is actually converted to fission energy, the remaining material is identified as spent nuclear fuel (SNF) and, rather than being considered for its potential energy, is discarded as waste. The technical issue thus falls to that of the breeding of Pu from the ^{238}U that constitutes the major component of the SNF.

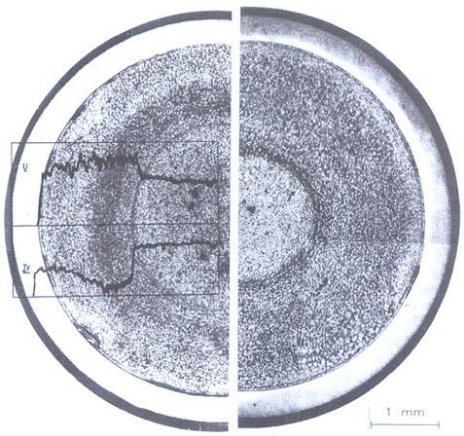

Figure 1. This is an example of site redistribution in U-10Zr (in wt.%) at 10 at.% peak burn-up. Being able to predict the phase and spatial morphology of an evolving fuel is a key to development of advanced reactors [1].

The burning of Pu and minor actinides raises the challenge of our lack of knowledge about the complex material itself, namely mixtures of U, Pu, and other minor actinides (MA) such as Np, Am, Cm, and Cf. Additionally, such complex mixtures evolve while the concentration of fission products (FP) increases in the reactor. To be successful, one must be able to model not only the physical properties of the complex mixture of actinides but also their evolution, including the

continuous in-growth of FP, and finally the interaction of the fuel itself with the cladding materials. The need for predictable evolution of the fuel is to a large extent a direct consequence of the need for higher burn-up, and is a concomitant challenge associated with closing the fuel cycle on the way to a sustainable nuclear strategy. For example the complex evolution of a metallic fuel during irradiation [1], shown in Fig. 1, requires the development of extensive thermodynamic and kinetic databases for the modeling to be predictive so effects such as decrease in fuel melting temperature, local fission rate change, site redistribution, and changes in swelling characteristics are predictable. Hence, the need for a paradigm shift that combines experiments with advanced theory, simulation, and modeling (TMS), to accelerate new fuel and reactor development and qualification in support of US energy security beyond the 20 years commonly agreed upon now [2].

Nuclear reactors used in the world to produce electricity have experienced continued technological improvements since their origin in the early 1950's. The current reactor fleet is of the 2nd and 3rd generations, and these are mainly light water (LWR) of either the Pressurized Water (PWR) or the Boiling Water (BWR) Reactor types in the US, Europe, and Japan, with analogs (VVER/PWR; RBMK/BWR) in Eastern countries, and CANDU (Heavy water reactors) in Canada and India. A new generation of reactors is poised to take over for the next 2 to 3 decades. The six selected options of the 4th generation (GEN-IV) that corresponds to the "systems of the future" still need to be conceived, and a deployment is envisioned around 2035 [3-5]. Gen-IV will require innovations well beyond the evolutionary developments of current systems, since future nuclear systems will not be limited solely to the production of electricity but also will face other requirements such as hydrogen production, and combined usage of heat production, *e.g.*, salt extraction from seawater or process heat for industry. Three main criteria of choice are part of the Gen-IV strategy, namely, preserving nuclear fuel resources, waste minimization, and proliferation resistance. Hence, innovation in fuel forms will include the entire list of actinides, U, Pu, and the minor actinides (MA), namely Np, Am, and Cm, from the used fuel to substantially limit the radio-toxicity of the ultimate waste, and better use the resources.

Most nuclear reactor concepts are currently based on Gen-III technology, and despite the push to go to higher burn-up, *i.e.*, from 0.6 to 9-10%, fuel development can still be considered evolutionary [2]. However, as nuclear science moves beyond Gen-IV [3], with advanced fuel initiatives (such as GNEP [4] and AFCI [5]), deep-burn [6], and hybrid fusion-fission concepts [7,8] (such as In-Zinarator [9], and FFTS [10]), high-performance fuels and containment

materials are critical path milestones which will require a definite revolutionary approach to fuel development beyond current methodologies [2].

To improve fuel performance for application in advanced reactor concepts, such as the sodium-cooled fast neutron spectrum nuclear reactor (SFR) of Gen-IV, several approaches have been considered that focus on increase in fuel content, lower temperature in the fuel element, extension of burn-up, and serviceability of the fuel elements operating under transient conditions. One of the most promising approaches is the compaction within a cladding material of actinide fuel particles infused by a metallic alloy [11], see Fig. 2. This fuel form is sound since the metallic matrix takes very little volume compared with the actinide fuel itself, and at the same time guarantees excellent heat transport, and has the potential to accommodate the swelling of the fuel kernel caused by fission gases (FG) production during burn-up thanks to the existence of the porous structure of the fuel form that acts as a built-in plenum. The requirement is that the matrix should be radiation resistant so that it maintains its thermal and mechanical integrity during the entire life of the fuel particle. In comparison with its oxide version, metallic inert matrix fuels (IMF) offer high effective fuel density and high thermal conductivity, efficient metallurgical bond between the fuel and the cladding, protection against fuel-cladding interaction, and uniform distribution of fuel particles in the metallic matrix.

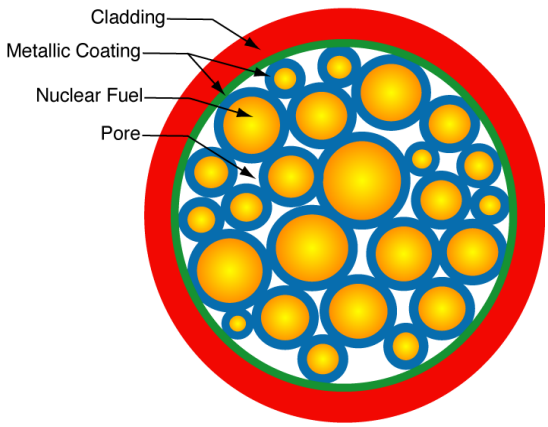

Figure 2. Schematic representation of an inert metal matrix fuel.

By adjusting the size of fuel granules, one can achieve high-fuel content, with volumes between 50 and 60% for the fuel “meat”, 7 and 15% for the metallic matrix, and 30 and 40% for the pores. It is also worth noting that the added solute elements (such as Fe and Cu) in the Zr metal matrix not only decrease the melting temperature of pure Zr by more than a factor 2, but also promote a natural beneficial coating (by the presence of high-melting point second-phase precipitation) of the cladding against reaction with fuel elements (U, Pu, and MA) and FP.

Our goal is to develop and validate with physics-specific experiments an integrated thermodynamic and kinetic modeling tool that can assess “in-core” ultra-high burn-up (UHBU) experiments on multi-phase microstructure evolution. In particular, this tool should predict the stability and time evolution of phase transformations and reactions associated with complex fuel materials exposed to a changing chemistry, and guide a high-throughput search for optimized

nuclear fuel compositions by monitoring micro-structural phase evolution in extreme conditions of radiation, temperature, and extended time. In the thermodynamic approach that forms the core of our phase diagram modeling, see Fig. 3, the Gibbs energy of individual phases is represented, and the model parameters are collected in a thermodynamic database from the assessment of available experimental data supplemented with electronic structure calculations within the framework of the CALPHAD (CALculation of PHAse Diagrams) methodology [12-16].

Here we employ three complementary computational techniques: (i) a scalar-relativistic (SR) Green function technique based on the Korringa–Kohn–Rostoker (KKR) method within the atomic-sphere approximation (ASA), (ii) scalar-relativistic and fully-relativistic (FR) exact muffin–tin orbital methods (EMTO), and (iii) the all-electron full-potential linear muffin–tin orbital method (FPLMTO) that also accounts for all relativistic effects. These methods have been developed to the point where reliable ground-state properties and energetics can be predicted for metallic alloys and actinides mixtures that will be discussed further in the next Section.

It is the modeling of the Gibbs energy of individual phases and the coupling of phase diagram and thermo-chemistry that make CALPHAD a powerful methodology in computational thermodynamics of multi-component materials. This CALPHAD representation of the Gibbs free energy feeds directly into a phase-field modeling code as the thermodynamic driving force.

To describe the alloy systems that are relevant for addressing phase formation and transformations in solid fuels in the presence of fissile and fertile nuclear fuels and FP, and the interaction between actinide fuel and metal inert matrix alloys, we are currently developing a

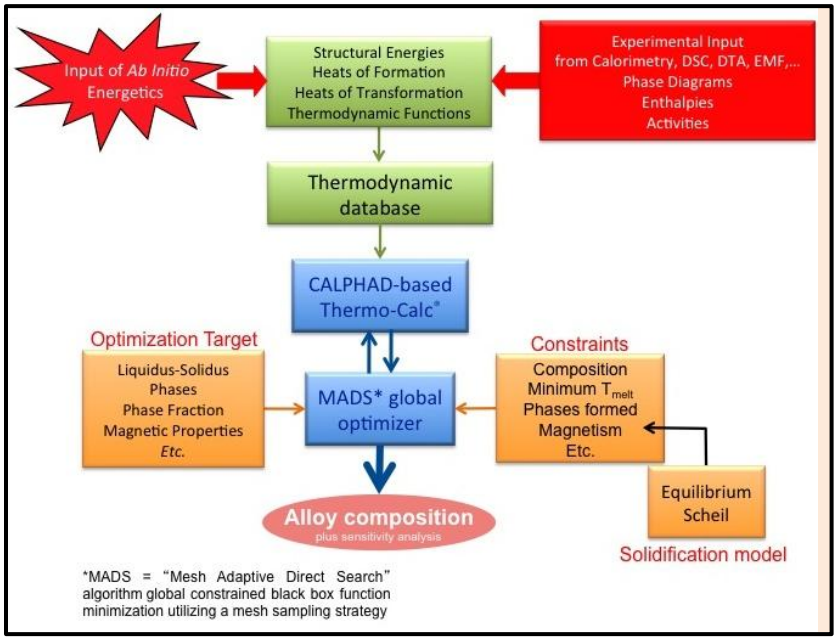

Figure 3. Schematic of the thermodynamic modeling of complex multi-component alloys.

thermodynamic database that includes the following elements {U, Np, Pu, Am} and {Al, Be, Cu, Fe, Mo, Nb, Si, Ta, Ti, W, Zr} for describing the actinide mixtures and the metallic inert matrix, respectively.

ELECTRONIC STRUCTURE APPROACHES

The series of actinide metals exhibit behaviors unlike any other elemental solids in the Periodic Table. Properties such as equilibrium volume (or density), crystal structure, phase stability, thermal and electrical transport, anisotropy, among others, make these materials exotic in comparison to most metals. Because of their scarcity, nuclear instability, toxicity, and regulatory requirements, experimental work is generally challenging to say the least. Nevertheless, great strides have been made in recent years to illuminate their nature from various experimental angles [17].

Theoretically, the actinides and actinide-based alloys pose a challenge as well due to complexities of the electronic and crystal structures, importance of relativistic effects, and the possibility of strong electron correlation. Hence, these systems have received increasing attention alongside technical developments of electronic band-structure methods [18] within the framework of density-functional theory (DFT) [19] and methods beyond DFT [20]. The implementation of conventional DFT methodologies have since evolved to better meet the challenges and accurately account for relativistic effects including spin-orbit interaction [21] and complex crystal structures [22].

The DFT band-structure approach is in principle only appropriate when dealing with bonding electrons that can be well described by band states. In the early actinide metals (and in nuclear metal fuel materials) this is indeed the case as we explain in Fig. 4. Here we plot the tabulated room temperature equilibrium volumes (full lines, no symbols) for the 5*d* transition metals, 4*f* lanthanides, and 5*f* actinides [23], together with two opposing models for the 5*f* character. The "5*f* fully bonding" model assumes band (delocalized) states, while in the other, "5*f* nonbonding" they are confined to core states with no band formation and interatomic bonding. Cleary, the former concept is justified for the earlier actinides Th-Np with plutonium showing a slight deviation. At the same time, the nonbonding model reproduces the behavior of the heavier actinides Am-Bk.

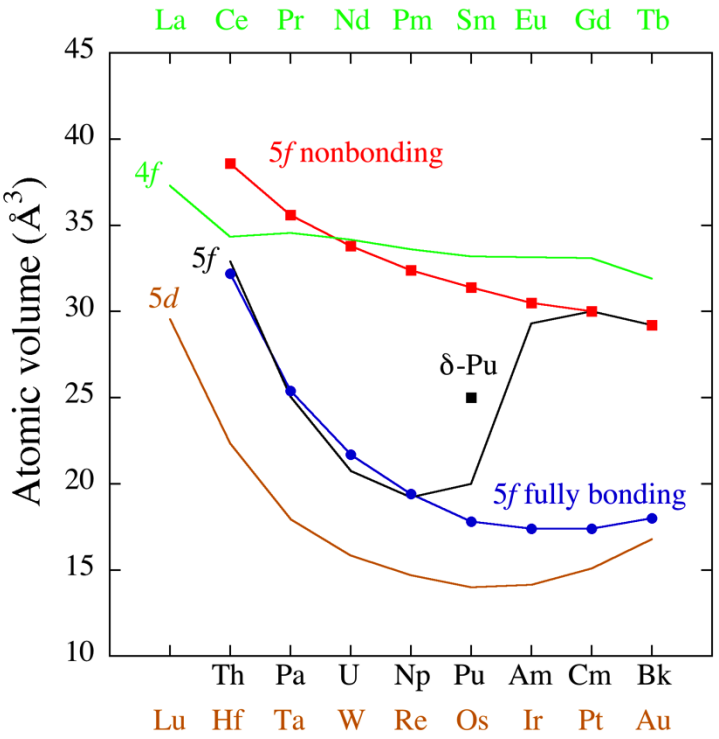

Figure 4. Measured atomic volumes of the actinide metals are shown with a black line (5*f*), a brown line for the 5*d* transition metals, and a green line for the lanthanides (4*f*). The blue "5*f* fully bonding" and red "5*f* nonbonding" curves show results from model calculations, assuming face-centered cubic structure, where the 5*f* electrons are treated as part of the valence band and localized to nonbonding core states, respectively.

These results confirm the notion that the early actinides have bonding (itinerant) 5*f* electrons while the later do not. This perception [24] was early founded on the fact that the 5*d* transition metals in Fig. 4 behave as the early and the 4*f* lanthanides as the late actinides. From Fig. 4 it is evident that the early and late actinides fall into two categories with respect to their atomic volumes and thus bonding strength of their 5*f* electrons. One of them, plutonium, appears to not quite fit either simplistic approach, particularly the (fcc-based) δ-Pu phase whose volume lies squarely in the middle between that predicted by the two bonding schemes. Consequently, numerous models have been proposed to particularly deal with δ-Pu [25]. These include "LDA+U" [26] as well as dynamical mean-field theory (DMFT) approaches [27]. Although useful to help describe the physics in some systems, these methodologies suffer from being unable to predict new phenomena due to their phenomenological construct with adjustable parameters. Furthermore, for practical purposes, this scheme cannot be made consistent for any alloy system that requires more than one "U" parameter, which is the case for multi-actinide alloys such as Pu-U-Zr. Nevertheless, the "LDA+U" approach has been applied for the metal nuclear fuel U-Zr where it was argued [28] to be important but this misunderstanding was later clarified [29].

Instead, we have focused our first-principles modeling on robust implementations of DFT for which consistent predictions can be made without the uncertainty of model parameters. Two

significantly different electronic-structure codes are utilized with complimentary strengths. The full-potential linear muffin-tin orbitals (FPLMTO) method do not compromise on accuracy beyond that necessary for the electron exchange and correlation energy functional, which is chosen to be the generalized gradient approximation (GGA) [30]. Although newer varieties of this approximation have been proposed, the GGA remains the best choice for actinide metals [31].

The other approach, the exact muffin-tin orbitals (EMTO) method, is well suited for alloy calculations because it allows for the coherent potential approximation (CPA) of the alloy system. Let us describe some of the more fundamental details of these two computational techniques.

Our particular FPLMTO approach is based on an implementation that has recently been described in detail [32]. In addition to the choice of GGA, we have found that for actinides no geometrical approximations (full potential), full relativity including spin-orbit coupling, spin and orbital polarization, and a well converged basis set is generally needed for the best accuracy. Specifically, we associate a set of semi-core states 6*s* and 6*p* and valence states 7*s*, 7*p*, 6*d*, and 5*f* to two kinetic energy parameters for a so-called double basis set. In all present calculations the sampling of k points in the Brillouin zone (BZ) for the appropriate summations are carefully checked for convergence. In order to simulate an alloy system the special quasi-random structure (SQS) [33] is used in conjunction with the FPLMTO.

The EMTO electronic-structure method that has been selected makes use of both scalar-relativistic and full relativistic Green's function techniques based on the improved screened Korringa-Kohn-Rostoker (KKR) method, where the one-electron potential is represented by optimized overlapping muffin-tin (OOMT) potential spheres [34]. Inside the potential spheres the potential is spherically symmetric, whereas it is constant between the spheres. The radii of the potential spheres, the spherical potentials inside the spheres, and the constant value in the interstitial region are determined by minimizing the deviation between the exact and overlapping potentials, and the errors caused by the overlap between the spheres. Within the EMTO formalism, the one-electron states are calculated exactly for the OOMT potentials. As an output of the EMTO calculations, one can determine the self-consistent Green's function of the system and the complete, non-spherically symmetric charge density. Finally, the total energy is obtained from the full charge-density technique [35].

We treat, as the valence states, the *7s*, *6p*, *6d*, and *5f* states for U, Np, Pu, and Am and *5s*, *4p*, and *4d* states for Zr, Nb, and Mo. The corresponding Kohn-Sham orbitals are expanded in terms of *spdf* exact muffin-tin orbitals, i.e. we adopt an orbital momentum cutoff, $l_{max} = 3$. The EMTO

orbitals, in turn, consist of the *spdf* partial waves (solutions of the radial Schrödinger equation for the spherical OOMT potential wells) and the *spdf* screened spherical waves (solutions of the Helmholtz equation for the OOMT muffin-tin zero potential). The completeness of the muffin-tin basis was discussed in details in Ref. [34], and it was shown that for metals crystallizing in close-packed lattices l_{max} = 3 (*spdf* orbitals) leads to the well converged charge density and total energy. For the electron exchange and correlation energy functional, the GGA is considered as in the case of the FPLMTO [30]. Integration over the Brillouin zone is performed using the special *k*-point technique [36]. The moments of the density of states, needed for the kinetic energy and valence charge density, are calculated by integrating the Green's function over a complex energy contour using a Gaussian integration technique with a semi-circle enclosing the occupied states. Spin-orbit interaction, when included, is obtained by solving the four-component Dirac equation [37].

In order to treat compositional disorder the EMTO method is combined with the CPA [36,37]. The ground-state properties of the chemically random alloys are obtained from EMTO-CPA calculations that include the Coulomb screening potential and energy [40-42]. The screening constants are determined from supercell calculations using the locally self-consistent Green's-function (LSGF) method [43].

Pu and Am containing alloys are treated as paramagnetic by the disordered-local-moment (DLM) model [44-46]. The equilibrium atomic density is obtained from a Murnaghan [47] fit to the total energy versus lattice constant curve (as is the case also for the FPLMTO calculations).

One should mention that our calculations on disordered bcc U-Zr, U-Np, and Np-Zr alloys were performed within the scalar-relativistic SR-KKR-ASA-CPA formalism instead of EMTO-CPA. The abbreviation KKR-ASA implies a Green's function technique based on the KKR method within the atomic sphere approximations (ASA) [47-50]. The SR-KKR-ASA formalism is well suited to treat close-packed structures for some U- and Np-based alloys but could produce a significant error when being applied to "open" structures such as C32 and $C11_b$ in U-Zr and U-Mo systems, respectively. In order to accurately model these structures, we applied EMTO formalism.

WHAT IS CALPHAD?

In the CALPHAD approach [12-15, 52, 53], the Gibbs energy of individual phases is modeled, and the model parameters are collected in a thermodynamic database. It is the modeling of the Gibbs energy of individual phases and the coupling of phase diagram and thermo-chemistry that

make the CALPHAD a powerful technique in computational thermodynamics of multi-component materials. Models for the Gibbs energy are based on the crystal structures of the phases. For pure elements and stoichiometric compounds, the most commonly used model is the one suggested by the Scientific Group Thermodata Europe (SGTE) [54] and has the following form (for simplicity, the pressure dependence and the magnetic contribution are not shown here),

$$G_m - H_m^{SER} = a + bT + cT\ln(T) + \sum d_i T^i \qquad (1)$$

The left-hand side of Eq. A.1 is defined as the Gibbs energy relative to a standard element reference state (SER), where H_m^{SER} is the enthalpy of the element in its stable state at 298.15 K and 1 bar of pressure. Coefficients, a, b, c, and d_i are the model parameters. The SGTE data for 78 elements of the Periodic Table have been compiled by Dinsdale [54].

For multi-component solution phases, the Gibbs energy has the following general expression [12-14,53],

$$G = G^o + G_{mix}^{ideal} + G_{mix}^{xs} \qquad (2)$$

where G^o is the contribution from the mechanical mixing of the pure components, G_{mix}^{ideal} is the ideal mixing contribution, and G_{mix}^{xs} is the excess Gibbs energy of mixing due to non-ideal interactions.

For a multi-component solution in a particular phase Φ described with a single sublattice model, the three contributions to the total Gibbs energy reduce to [13,14,53]:

$$\begin{aligned} {}^{\Phi}G^o &= \sum_I c_I \, {}^{\Phi}G_I^o \\ {}^{\Phi}G_{mix}^{ideal} &= RT\sum_I c_I \ln c_I \\ {}^{\Phi}G_{mix}^{xs} &= \sum_I \sum_{J>I} c_I c_J \sum_k {}^{\Phi}L_{I,J}^k (c_I - c_J)^k \end{aligned} \qquad (A3)$$

The molar Gibbs energy of mixing is expressed by a Redlich-Kister expansion [55]. In these expressions c_I is the composition of the alloy in species I, and the $L_{I,J}^k$ is the k^{th}-order binary interaction parameter between species I and J usually expressed as a first-order polynomial in temperature T: $L_{I,J}^k = a_{I,J}^k + b_{I,J}^k T$. Note that in both sets of expressions the excess Gibbs energy due to non-ideal contributions is expressed within the Muggianu approximation [56].

For line compounds, the total Gibbs energy is a simple expression such as:

$$^{F}G = \sum_{I} c_I \, {}^{Ref}G_I^0 + A + BT + CT\ln T$$

where ${}^{Ref}G_I^0$ is the Gibbs energy of species I, with composition c_I, that makes up the compound in a particular reference state (*i.e.*, structure), is generally adopted.

Within the CALPHAD approach, more complex models have been proposed to describe various mixtures, particularly the ionic model and the sublattice models, the latter being generalized for phases with multi-components and multi-sublattices [13, 14, 53], that reduce to a random substitutional model when there is only one sublattice.

Data generated with the Thermo-Calc software also provide the basis for more accurate predictions of diffusion kinetics and ultimately TTT (temperature-time-transformations) diagrams with the DICTRA software [57, 58] by assuming diffusion both in the liquid and the solid phase. Note that the results of both equilibrium solidification and Scheil-Gulliver simulations generated by Thermo-Calc correspond to upper and lower bounds for the DICTRA results. Input data files used by Thermo-Calc are: KP (Kaufman binary alloys database), SSOL4 (Scientific Group Thermodata Europe, or SGTE, solution database), from published journals, and/or from qualified sources. Here, to describe the selected alloys systems, a thermodynamic database has been developed.

AB INITIO RESULTS FOR SELECTED ACTINIDE-BASED ALLOYS

Figure 5a shows results of our SR-KKR-ASA-CPA calculations of the heat of formation of γ-U-Zr (bcc) solid solutions at T = 0 K [59, 60]. The heat of formation, that shows a positive deviation from the energy associated with a mixture of the pure elements, agrees well with the existence of a miscibility gap in the U-Zr phase diagram. Notice that the calculated heat of formation of γ-U-Zr solid solutions is in excellent accord with data derived from a CALPHAD assessment [61, 62] of the experimental thermodynamics and phase diagram information, thus validating the *ab initio* approach. Note that to have a consistent comparison between the *ab initio* and CALPHAD results, the heat of formation within CALPHAD is extrapolated at T = 0 K. For comparison, we also show the heats of formation for $U_{75}Zr_{25}$, $U_{50}Zr_{50}$, and $U_{25}Zr_{75}$ bcc alloys, calculated within the FPLMTO-SQS technique that compares well with both SR-KKR-ASA-CPA and CALPHAD assessment results.

Figure 5b shows results of EMTO-CPA calculations of the heat of formation of the γ-U-Mo solid solutions at T = 0 K [63, 64]. It is positive in a broad region of the composition interval and

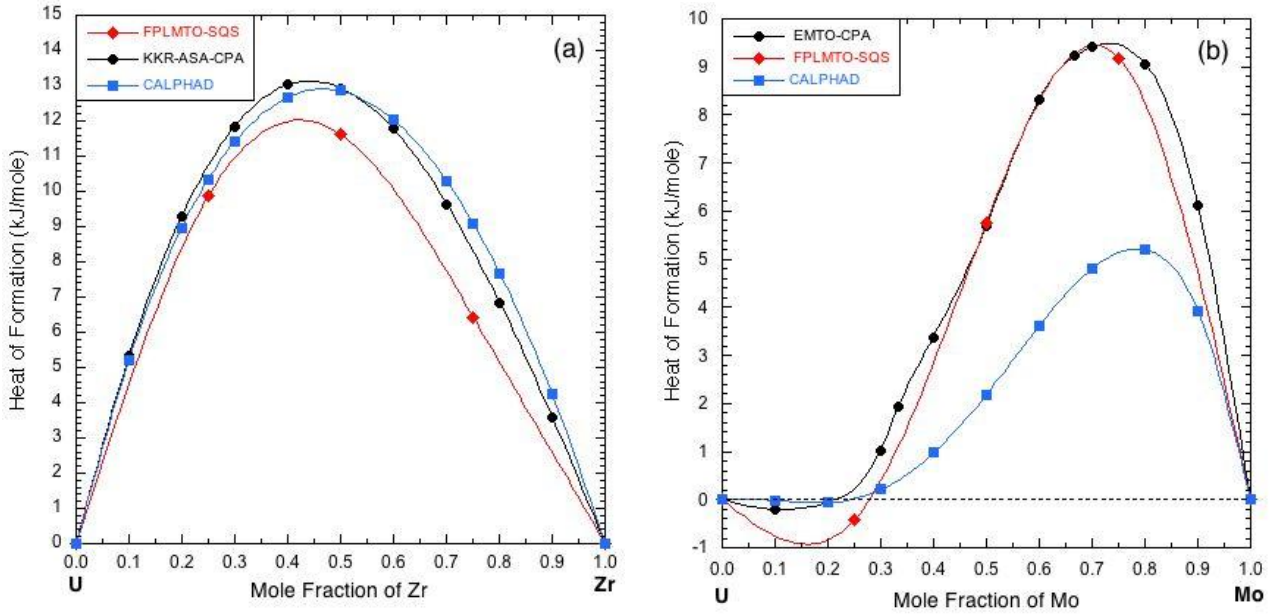

Figure 5. The heat of formation versus composition calculated at T = 0 K for (bcc-based): (a) γ-U-Zr and (b) γ-U-Mo alloys. The full lines are guides to the eye only.

changes sign when uranium composition exceeds ~80 at. %. For comparison, we also show the heats of formation for the $U_{75}Mo_{25}$, $U_{50}Mo_{50}$, and $U_{25}Mo_{75}$ bcc alloys [63, 64], calculated within the FPLMTO-SQS technique that again agrees relatively well with EMTO-CPA results. This plot also shows CALPHAD assessment [65] of the heat of formation of the γ-U-Mo solid solutions at T = 100 K with a distinctive change of its sign from positive to negative around 80 at. % of uranium.

In an earlier paper [63] we compared the heat of formation of bcc U-Zr and U-Mo solid solutions and explained why decomposition takes place for γ-U-Zr alloys that, in turn, causes higher constituent redistribution in U-TRU-Zr fuels than in U-TRU-Mo fuels (TRU=TRansUranic element) where a single γ-phase field exists. In Figure 6 we show this together with new results for the U-Nb bcc alloys (EMTO-CPA), thus completing the study of bcc solution of uranium with 4*d* transition metals.

In previous papers [59, 60, 66-68] we performed calculations of the heat of formation of bcc-based γ-X-Zr (X = U, Np, Pu, Am) solid solutions. We discovered that calculated heats of formation of the γ-U-Zr, γ-Np-Zr, and γ-Pu-Zr alloys are in a good agreement with data derived

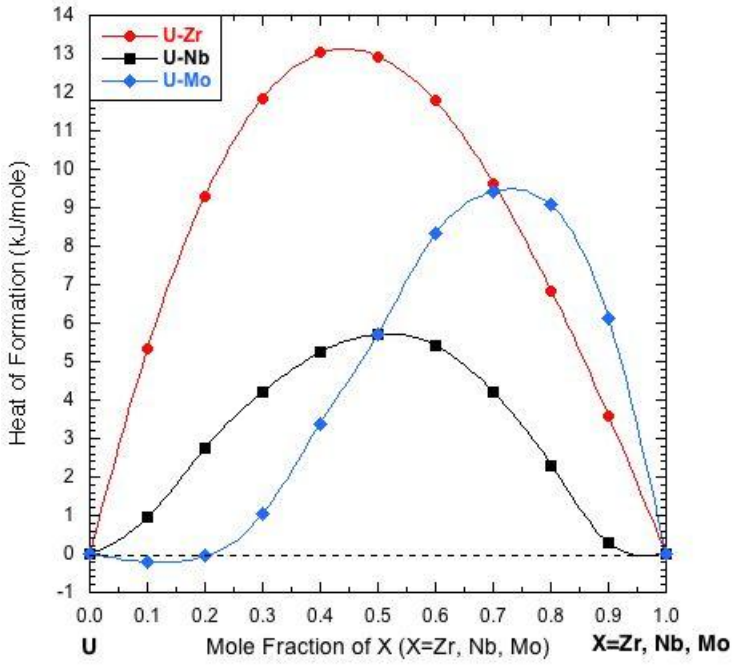

Figure 6. The heat of formation versus composition calculated at T = 0 K for: (bcc-based) γ-U-Zr, γ-U-Nb, and γ-U-Mo alloys. The full lines are guides to the eye only.

from a CALPHAD assessment [61, 62] of the experimental thermodynamics and phase diagram information for these systems, although we could not perform the corresponding assessment in the case of the Am-Zr system due to the complete lack of experimental thermodynamics data and absence of phase diagram.

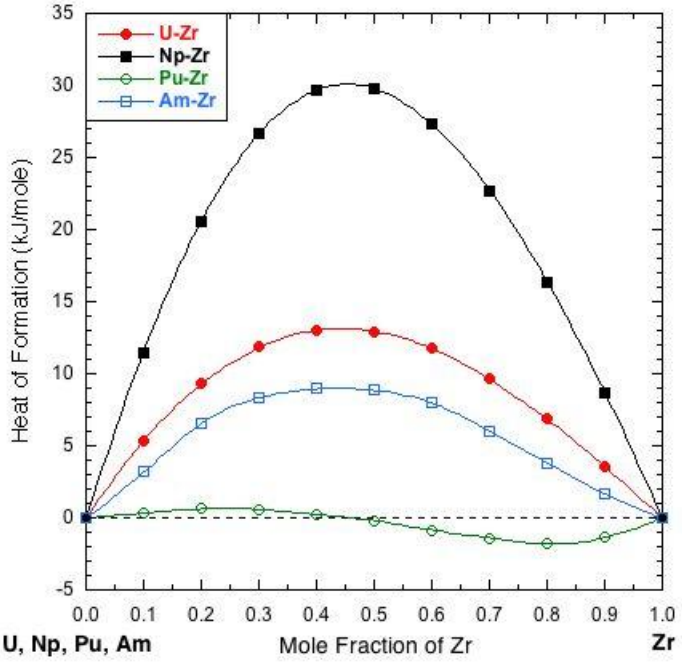

Figure 7. The heat of formation versus composition calculated at T = 0 K for (bcc-based) γ-X-Zr (X = U, Np, Pu, Am) alloys. The full lines are guides to the eye only.

The results of calculated (SR-KKR-ASA-CPA and EMTO-CPA) heat of formation of bcc-based γ-X-Zr (X = U, Np, Pu, Am) solid solutions are shown in Fig. 7 that also agree relatively well with results of FPLMTO-SQS calculations [59, 60, 66-68] (not shown). For non-magnetic (NM) solutions the heat of formation increases in sequence γ-U-Zr → γ-Np-Zr and remains positive within the whole compositional interval. For paramagnetic (PM) or DLM γ-Pu-Zr solid solutions the heat of formation changes sign in the vicinity of the equi-atomic composition but its absolute value remains very small, probably due to the insignificant difference between the equilibrium atomic volumes of bcc Pu and Zr. For PM γ-Am-Zr solid solutions the heat of formation stays positive within the whole compositional interval and is significantly larger than the absolute value of the heat of formation of γ-Pu-Zr solid solutions due to the larger mismatch between the equilibrium atomic volumes of bcc Am and Zr.

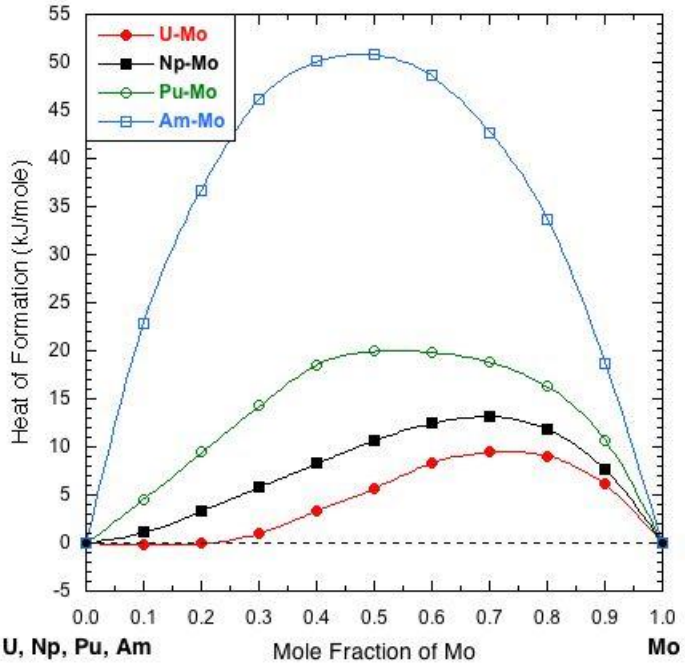

Figure 8. The heat of formation versus composition calculated at *T* = 0 K for (bcc-based) γ-X-Mo (X = U, Np, Pu, Am) alloys. The full lines are guides to the eye only.

Figure 8 shows results of our calculations (EMTO-CPA) of the heat of formation of bcc-based γ-X-Mo (X = U, Np, Pu, Am) solid solution [64]. The magnitude of heat of formation of these solutions increases in the sequence: γ-U-Mo → γ-Np-Mo (both NM) → γ-Pu-Mo → γ-Am-Mo (both PM). For γ-X-Zr alloys, mentioned above, the equilibrium atomic volume of bcc Zr is larger than that of bcc U and Np but smaller than that of bcc Pu and Am. This is different to the γ-X-Mo alloys where the equilibrium volume of bcc Mo is smaller than that of bcc U, Np, Pu,

and Am. The difference in volumes of the components explains the aforementioned sequence depicted in Figure 8. One should also point out that these results are consistent with results from FPLMTO-SQS calculations [64] (not shown).

In Figure 9 we display results of our calculations (EMTO-CPA) of the heat of formation of bcc-based γ-X-Am (X = U, Np, Pu) solid solution [68-70] These are in good accord with that from FPLMTO-SQS calculations, and particularly good agreement is found for γ-Pu-Am [69]. For all

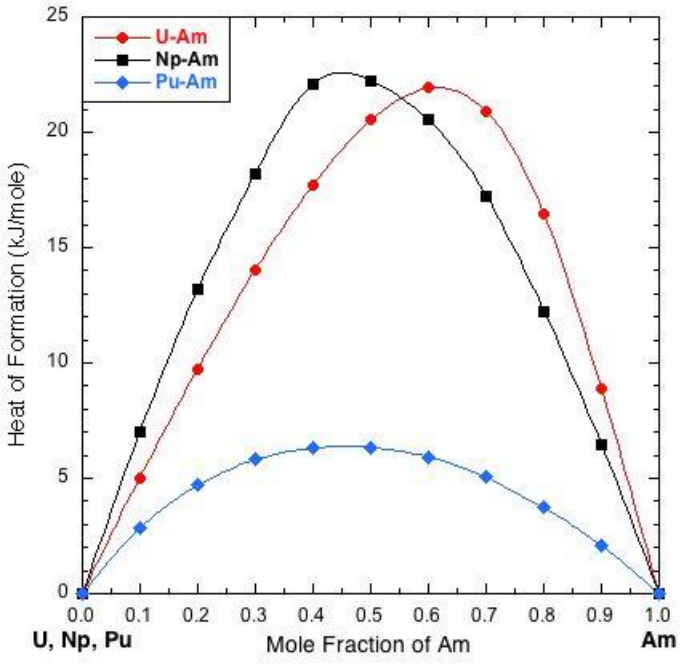

Figure 9. The heat of formation versus composition calculated at T = 0 K for (bcc-based) γ-X-Am (X = U, Np, Pu) alloys. The full lines are guides to the eye only.

these alloys the heat of formation is positive, identical in magnitude for γ-U-Am and γ-Np-Am alloys but significantly smaller for γ-Pu-Am alloys. We explain this to be due to the lesser equilibrium-volume mismatch between components of Pu-Am system relative to the U-Am and Np-Am alloys.

Finally, Fig. 10 shows results of our calculations (EMTO-CPA) of the heat of formation of bcc-based γ-U-X (X = Np, Pu, Am) solid solution [68, 69]. The heat of formation for γ-U-Np solid solution is small and positive and in the case of γ-U-Pu solid solution the heat of formation is negative, in excellent agreement with data derived from a CALPHAD assessment [61, 62] (see Ref. [68] for details). For γ-U-Pu solid solution results of EMTO-CPA calculations and CALPHAD assessment agree pretty well with results of FPLMTO-SQS calculations [68].

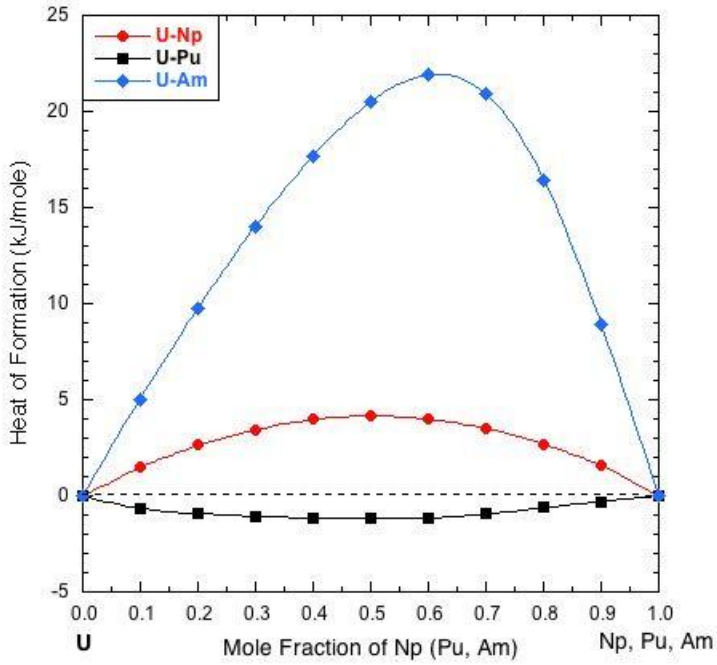

Figure 10. The heat of formation versus composition calculated at T = 0 K for (bcc-based) γ-U-X (X = Np, Pu, Am) alloys. The full lines are guides to the eye only.

AB INITIO INFORMED PHENOMENOLOGICAL CALPHAD-BASED THERMODYNAMIC MODELING

1. PHASE DIAGRAM OF THE Mo-Pu ALLOY SYSTEM

A Mo-Pu phase diagram of the simple eutectic type has been published by Bochvar *et al*. [69] in the late fifties, with an eutectic invariant line located at 590 ^{o}C. Later, the eutectic temperature was revised between 625 ^{o}C [72, 73], and 613 ^{o}C [74]. It was verified that no intermediate phases in as-cast alloys were found, and a liquidus point at 26 at.% Mo and 1750 ^{o}C was measured [75]. The solubility of Mo in liquid Pu between 700 and 1000 ^{o}C was determined later [76]. Based on these limited experimental data Brewer *et al.* [77] applied their phenomenological modeling to assess the thermodynamic data of the liquid and bcc phases of Mo-Pu.

Hence, besides the assessed values of the Gibbs energies of the pure species in their various allotropic forms, the only experimental results are: the position of the eutectic invariant line at 613 ^{o}C [74], and the Mo solubility in liquid Pu versus temperature [75, 76]. Since no experimental information is available for the heats of transformation or other thermodynamic data as functions of composition and temperature, *ab initio* calculations were carried out with the FR-EMTO-CPA code with computational details outlined above. The results for the heat of formation and equilibrium properties (lattice parameter and bulk modulus) of chemically random

bcc-based Mo-Pu alloys as a functions of composition are summarized in Figure 11. The bcc phase of Mo-Pu clearly exhibits a strong tendency towards phase separation with a maximum positive heat of formation of about 20.5 kJ/mole around 60 at.% Mo, also reflected in the negative deviation from linearity of the bulk modulus (associated with a loss of cohesion).

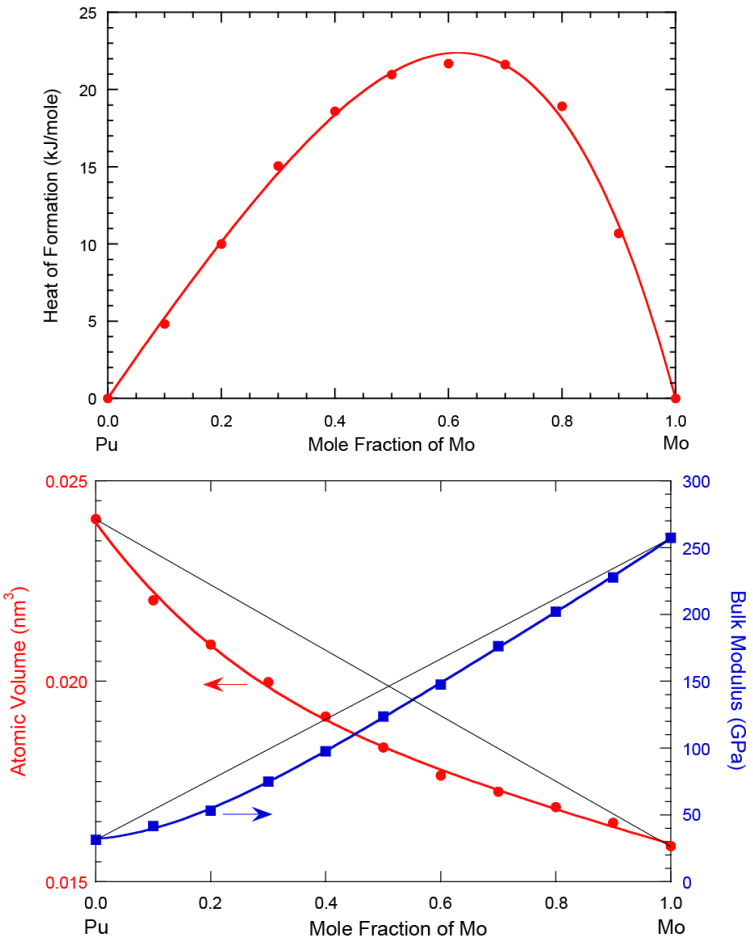

Figure 11. *Ab initio* results from FR-EMTO-CPA method of heat of formation (top) and volume and bulk modulus (bottom) for bcc-based chemically random Mo-Pu alloys at T=0 K. In the top figure, the line is obtained from a Redlich-Kister polynomial fit.

However, contrary to the normal situation, the volume versus alloy composition displays a negative deviation from Zen's law (usually associated with a tendency towards order).

The heat of formation versus composition curve was then fitted by a two-terms Redlich-Kister polynomial [55] that describes the excess Gibbs energy of the bcc phase of Mo-Pu at zero temperature. Hence, with the extra information on the energetics of the bcc phase of Mo-Pu, a thermodynamic assessment was carried with the optimization module of Thermo-Calc [57] to provide all the Gibbs energies versus temperature and alloy composition that are necessary to predict the final phase diagram shown in Figure 12.

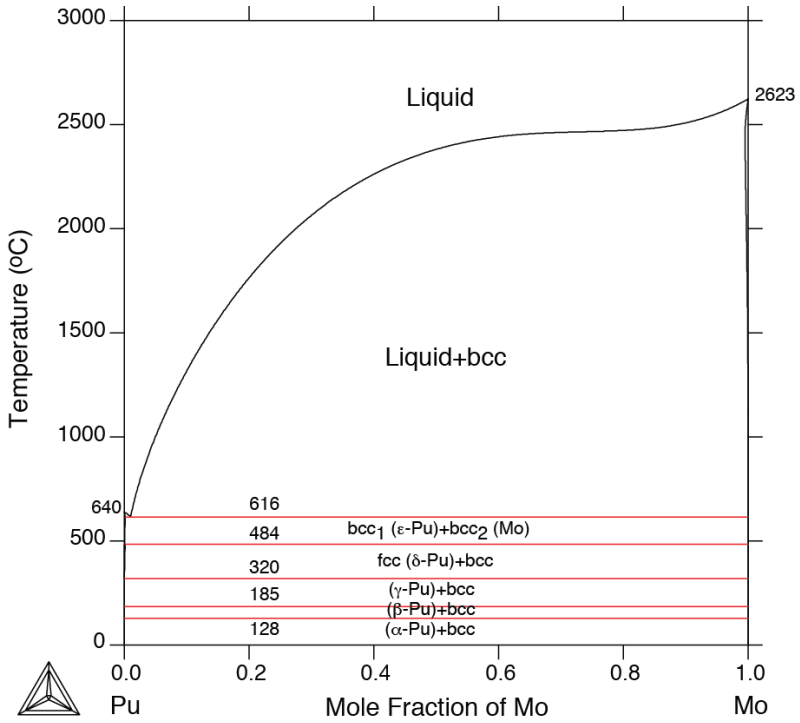

Figure 12. Thermodynamic re-assessment of the Mo-Pu phase diagram based on the *ab initio*-CALPHAD methodology.

2. PHASE DIAGRAM OF THE Am-Pu ALLOY SYSTEM

With the current interest in Gen-IV advanced nuclear reactors [3-5] and an improved management of actinide-based fuels, and in the disposition of transuranic elements (TRU), there is a need to better understand the thermodynamic properties of mixtures of actinide elements. In particular, since the amount of Am in Pu in the next generation of actinide burner reactors may be significant, it becomes increasingly important to include Am in a thermodynamic database dedicated to nuclear fuel materials to understand its impact on the stability properties of Pu-based alloys. For this particular system, a detailed study of it has been reported elsewhere [70], only two phase diagrams are known that are distinguished by the existence of at least one peritectic reaction on the Pu side [78] or a bcc phase in the entire range of alloy composition [79-81].

Once again with input energetics from *ab initio* electronic structure calculations shown in Figure 9 [68, 69], and the few sparse information on phase diagram thermodynamic assessment was carried out. The predicted phase diagram of Am-Pu shown in Fig. 13 (top) accounts for the existence of a high-temperature bcc solid solution, and a domain of stability of a dhcp (A3')-based solid solution in the Am rich-side of the phase diagram, with a two-phase region (fcc+dhcp), in accordance with the findings of Ref. [79], and as expected from the fundamental laws of thermodynamics. The addition of less than 1 kJ/mole (at equi-atomic composition) to the

excess Gibbs energy of the high-temperature bcc phase leads to a phase diagram, see Fig. 13 (bottom) that is in agreement with the one proposed in Ref. [78].

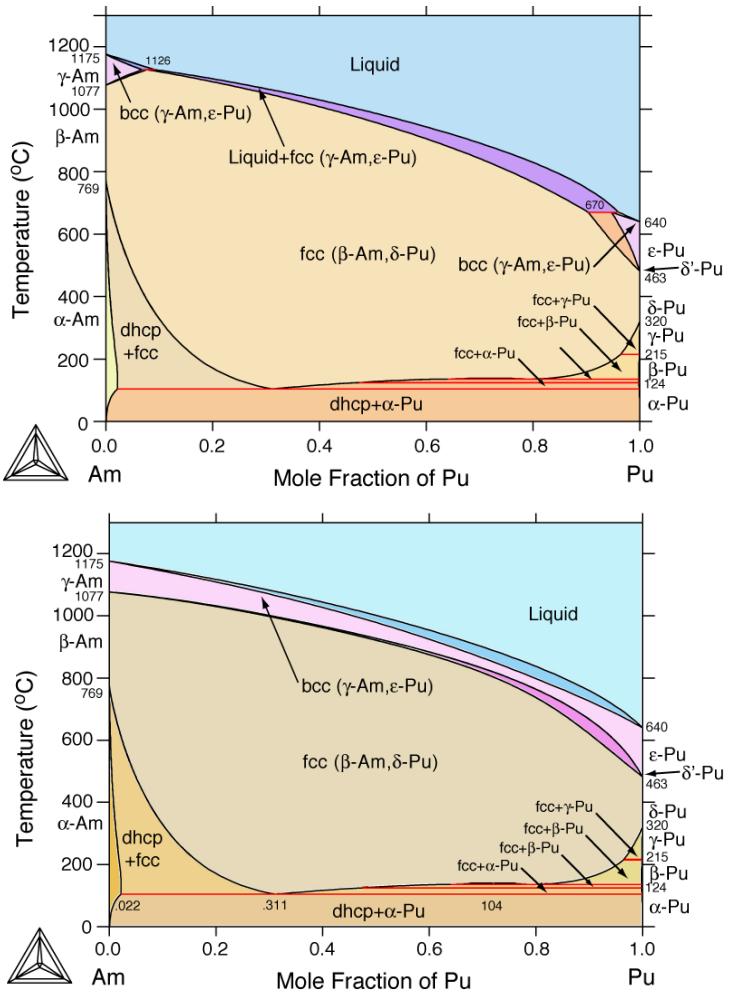

Figure 13. Thermodynamic re-assessment of the Am-Pu phase diagram based on the *ab initio*-CALPHAD methodology, in accord with the experimental data from Refs. [79] (top), and [78] (bottom).

This study indicates that the high-temperature part of the Am-Pu phase diagram is extremely sensitive to the thermodynamic data and hence to the impurity content, and it would hard to conclude which one of the two is the best representative of the stability properties of the Am-Pu system.

Further improvement to the thermodynamic description of this system, as it is true for many actinide-based alloys that have not been re-assessed with modern experimental techniques, will require additional experiments, in particular differential scanning calorimetry (DSC) and differential thermal analysis (DTA) combined with high-temperature X-ray structure analysis and transmission electron microcopy for phase characterization. However, this study provided some initial thermodynamic data for this system that can also be compared with other theoretical

modeling. Since sample preparation is challenging, CALPHAD assessments allow us to select some alloy compositions, namely around 80 and 90 at.% Pu in the case of Am-Pu, to further confirm the existence or not of a domain of stability of a bcc solid solution in the entire range of alloy composition or a peritectic reaction, respectively. It is worth mentioning that useful guidance by CALPHAD for DTA and DSC measurements can be provided [70] for making a definite choice between the two proposed phase diagrams and consequently validating the *ab initio*-informed CALPHAD approach.

3. EXTENSION TO THERMODYNAMIC PROPERTIES OF MULTI-COMPONENT SYSTEMS

The promise of the CALPHAD approach is mostly in its ability to extend the assessment done for binaries to multi-component systems. Actually, there is a necessity for results of CALPHAD assessments of binary systems to be confronted to experimental results obtained for at least ternary combinations. However, in the case of actinide-based systems, very few studies have been made on multi-component systems, and therefore, CALPHAD results once again can only guide future experimental work or at least predict derived properties, such as phases and melting temperature at a given alloy composition. Let us first consider the case of the ternary Mo-Pu-U system that is of great interest to the RERTR (GTRI) international program. By assembling the thermodynamic data for Mo-Pu [82], Mo-U [83] and Pu-U [62], isothermal section of the ternary phase diagram are shown in Fig. 14. From these results it can be noted that down to about 1073 K (800 ^{o}C) the domain of stability of the bcc (γ) phase that prevails in the Mo-U system at high uranium composition still exists. However, at lower temperatures, other phases stabilized by the presence of plutonium start forming. Hence, the conclusion that the addition of Pu to the Mo-U system reduces the domain of stability of the highly desirable bcc phase.

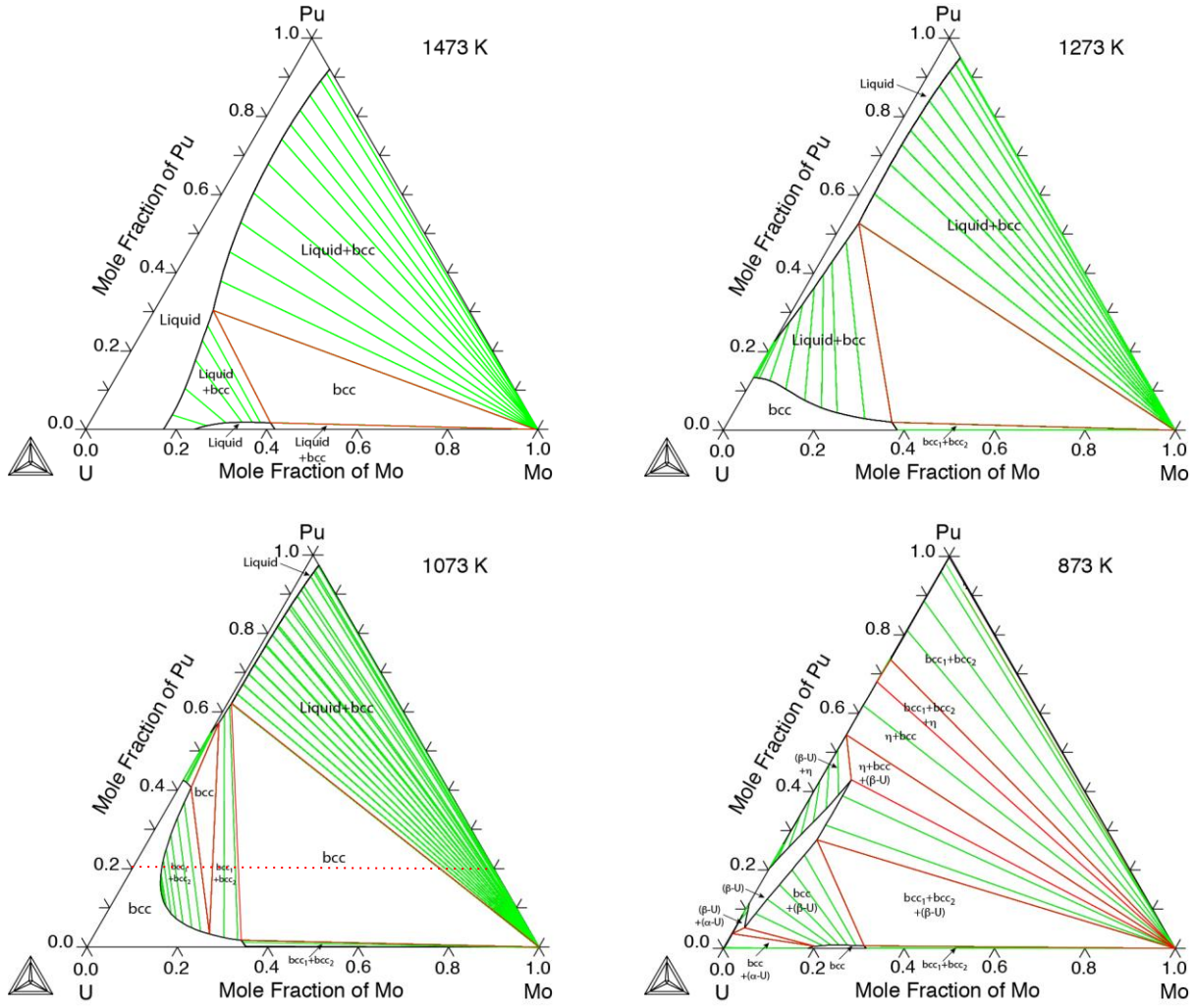

Figure 14. Predicted isothermal sections of the Mo-Pu-U phase diagram from 1473 to 873 K (1200-600 ^{o}C).

As a second example, by adding Al and Si to the previous thermodynamic database, one can start studying the interaction of the fuel (Mo, Pu, U) with the cladding materials (Al, Si). It has been reported in Ref. [84] that considering two Al-Mo-U alloys, $Al_{85.7}Mo_{2.86}U_{11.44}$ and $Al_{87.5}Mo_{2.5}U_{10}$ (in at.%), the phases that are observed are fcc (Al-rich) solid solution, Al_4U, Al_3U, $Al_{43}Mo_4U_6$ and $Al_{20}Mo_2U$, except that for the second alloy the Al_3U is not observed. Using our thermodynamic database the property diagram of each of these two alloys was calculated [85]. As a reminder, for a complex multi-component alloy at a specific alloy composition, the property diagram conveniently shows the phase fraction of each phase that forms as a function of temperature. This can be directly compared with experimental results, and as such constitutes a way of validating a thermodynamic database. In Figure 15, the property diagram of each of the mentioned alloys is shown [85]. It is notable that the first phases to form are Al_3U and

$Al_{43}Mo_4U_6$, and the phase fraction of Al_3U is lower for the slightly lower U-content alloy (right panel): This may explain why for this alloy this Al_3U phase is more difficult to observe. Also, one should note that crystallization occurs at similar temperatures, of about 1600 ^oC whereas the last drop of liquid is observed down to 641 ^oC, hence a huge undercooling in these alloys. This has consequences on how alloys at these compositions should be treated as functions of temperature to ensure that true phase equilibrium is observed. Finally, the phases that sequentially form below the liquidus surface are, in order of decreasing temperatures: $Al_{43}Mo_4U_6$ – Al_3U – $Al_{20}Mo_2U$ – {Al_4U, fcc solid solution}. These findings are in agreement with those reported in Ref. [85] that for the two Al-Mo-U alloys considered in the modeling, namely $Al_{85.7}Mo_{2.86}U_{11.44}$ and $Al_{87.5}Mo_{2.5}U_{10}$ (in at.%), where the phases that are observed are fcc (Al-rich) solid solution, Al_4U, Al_3U, $Al_{43}Mo_4U_6$ and $Al_{20}Mo_2U$, except that for the second alloy the Al_3U is not observed.

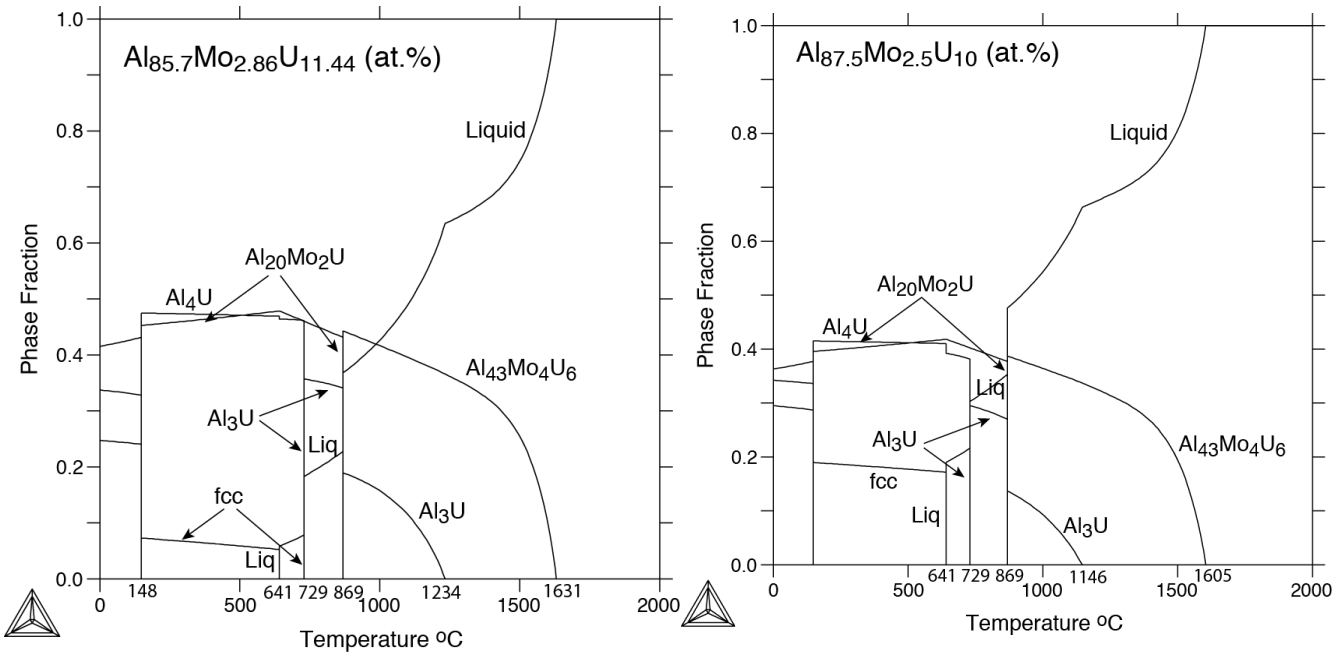

Figure 15. Based on a CALPHAD assessment of the thermodynamic properties of Al-Mo-U system, the property diagrams of $Al_{85.7}Mo_{2.86}U_{11.44}$ (left) and $Al_{87.5}Mo_{2.5}U_{10}$ (right), in at.% are shown.

APPLICATION OF THERMODYNAMICS TO ALLOY DESIGN

Once a thermodynamic database has been constructed and (preferably) validated by experimental data for the binary and possibly the ternary subsystems, the search in the multi-composition space for an alloy with, for example, desirable melting temperature and proper phases that form

as functions of temperature, can proceed with the scheme displayed in Fig. 3 with the help of a search engine [86], in the present case a global optimizer based on an updated version of the Mesh Adaptive Direct Search (MADS) algorithm [87]. To illustrate the power of this additional tool, let us consider the following multi-component system {Cu, Fe, Ti, Zr} as a subset of a more complex six-component system that would also include {Be, Nb}, and for which a thermodynamic database has been assembled and validated. For this quaternary alloy, the use of the engine for searching the minimum melting temperature in the multi-composition space with a large fraction of ductile phase leads to the following composition: Cu (4.8)-Fe (17.2)-Ti (15.8)-Zr (62.2) (in wt.%) with a melting temperature 823 ^{o}C, and the first phase to crystallize in large quantity out of the melt is body-centered cubic with a small fraction of compounds, as shown in Fig. 16. This application can be advantageously used to identify proper alloy compositions for the coating materials [88] that is used for designing the inert matrix fuel (IMF) [11] discussed in the Introduction, and shown in Fig. 2. Another application for this tool that is currently considered is to identify an optimum alloy composition for the multi-component system made of {U, Mo, Nb, Ti, Zr} that leads to an increase of the solidus temperature and, at the same time, to a lowering of the onset temperature of the bcc phase to extend fuel reliability to ultra-high burn-up [89].

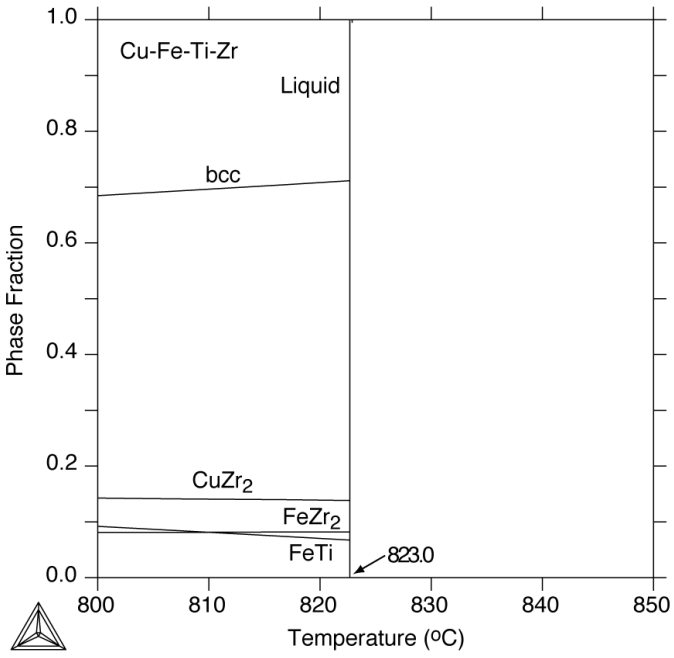

Figure 16. Property diagram (phase fraction versus temperature) of a Cu-Fe-Ti-Zr alloy whose composition has been identified (see text) to lead to the lowest melting temperature of about 823 ^{o}C in the multi-composition space.

CONCLUSIONS

Our work is geared towards establishing the basic science of a transformational high-throughput protocol for the development and qualification of advanced nuclear fuels that relies on modern computational materials modeling and simulation tools. The goal is to create the fundamental scientific basis for the complex evolution of UHBU advanced nuclear energy fuel systems driven far from equilibrium, and improve fuel development and qualification process to enable rapid, cost effective decisions from a fully validated and integrated science-based platform. This "ideal to real" strategy for the development of the next generations of advanced nuclear energy systems starts with the development of a validated thermodynamic database for actinide-based alloys (and also cladding materials) that is accomplished by combining state-of-the-art *ab initio* electronic-structure calculations and phenomenological CALPHAD thermodynamic assessments. The few examples that were selected for this paper show that the predictions, since in most cases the experimental data available for this class of alloys are sparse, allow us to study multi-component alloys, and if nothing else, guide experimental investigations that are usually difficult and costly. Not only binary phase diagrams, but also isothermal sections of ternary phase diagrams, and pseudo-binary phase diagrams, as well as property diagrams can be calculated, in addition to data that directly relate to experimental measurements such as those obtained with high-temperature calorimetry and DSC. It is also important to emphasize the relevance of the CALPHAD methodology for dealing with multi-component alloy systems and the few examples that were given demonstrate how this can help to design materials with improved properties. Finally, the predicted thermodynamic driving forces, combined with species mobilities (*i.e.*, diffusion data) can be used as input for upper-scale modeling, and in particular with coarse-grained phase-field modeling to study the impact of microstructure evolution on nuclear fuel behavior and performance under normal and accidental conditions.

ACKNOWLEDGMENTS

This work was performed under the auspices of the U.S. Department of Energy by Lawrence Livermore National Laboratory under contract DE-AC52-07NA27344. Work at LLNL was funded by the Laboratory Directed Research and Development Program under project tracking code 12-SI-008.

REFERENCES

[1] G.L. Hofman, S.L. Hayes, and M.C. Petri, J. of Nucl. Mater. **227**, 277-286 (1996).

[2] D.C. Crawford, D.L. Porter, S.L. Hayes, M.K. Meyer, D.A. Petti, and K. Pasamehmetoglu, J. of Nucl. Mater. **371**, 2321-242 (2007).

[3] Nuclear Energy Research Advisory Committee and The Generation IV International Forum, A Technology Roadmap for Generation IV Nuclear Energy Systems, US DOE Report, December 2002; US DOE Office of Nuclear Energy, Science and Technology, The US Generation IV Implementation Strategy, US DOE Report (Sept. 2003); J. Couturier *et al*., "Réacteurs de quatrième generation – Notes de Synthèse", IRSN-2007/91-FR Report (21 Nov. 2007).

[4] "Global Nuclear Energy Partnership Strategic Plan", US DOE Report No. GNEP-167312, Rev. 0 (2007).

[5] Report to Congress on the Advanced Fuel Cycle Initiative, US DOE Report (2003).

[6] R.M. Versluis, F. Venneri, D. Petti, L. Snead, and D. McEachern, "Project deep-burn: development of transuranic fuel for high-temperature helium cooled reactors", Proceedings of the 4th International Topical Meeting on High-Temperature Reactor Technology", HTR2008-58325 (4 pages), Sept. 28-Oct. 1, 2008, Washington DC.

[7] T.A. Mehlhorn, B.B. Cipiti, C.L. Olson, and G.E. Rochau, "Fusion–fission hybrids for nuclear waste transmutation: A synergistic step between Gen-IV fission and fusion reactors", Fusion Engineering and Design (2008), 6 pages.

[8] Wallace Manheimer, J. of Fusion Energy **23** (4), 223-235.

[9] Fusion Transmutation of Waste: Design and Analysis of the In-Zinerator Concept", Sandia Report SAND2006-6590 (Nov. 2006)

[10] M. Kotschenreuther, P.M. Valanju, S.M. Mahajan, and E.A. Schneider, "Fusion–Fission Transmutation Scheme – Efficient destruction of nuclear waste", Fusion Energy and Design **84**, 83-88 (2009).

[11] A.M. Savchenko, A.V. Vatulin, E.M. Glagovsky, I.I. Konovalov, A.V. Morozov, A.V. Kozlov, S.A. Ershov, V.A. Mishunin, G.V. Kulakov, V.I. Sorokin, A.P. Simonov, Z.N. Petrova, and V.V. Fedotov, J. of Nucl. Mater. **396**, 26-31 (2010); and references therein.

[12] L. Kaufman and H. Bernstein, "*Computer Calculation of Phase Diagrams with Special Reference to Refractory Metals*" (Academic Press, New York, 1970).

[13] N. Saunders and A. P. Miodownik, "*CALPHAD, Calculation of Phase Diagrams: A Comprehensive Guide*", Pergamon Press (1998).

[14] "*CALPHAD and Alloy Thermodynamics*", ed. by P. E. A. Turchi, A. Gonis, and R. D. Shull (TMS Publication, Warrendale, PA, 2002); and references therein.

[15] MRS Bulletin, Vol. **24**, No. 4 (April 1999), "*Computer Simulations from Thermodynamic Data: Materials Production and Development*", p. 18-49.

[16] P.E.A. Turchi, I.A. Abrikosov, B. Burton, S.G. Fries, G. Grimvall, L. Kaufman, P. Korzhavyi, V.R. Manga, M. Ohno, A. Pisch, A. Scott, and W. Zhang, CALPHAD **31**, 4-27 (2007).

[17] K.T. Moore and G. van der Laan, Rev. of Modern Phys. **81**, 235 (2009).

[18] H.L. Skriver, O.K. Andersen, and B. Johansson, Phys. Rev. Lett. **41**, 42 (1978).

[19] P. Hohenberg and W. Kohn, Phys. Rev. **136**, B864 (1964); W. Kohn and L. Sham, Phys. Rev. 140, A113 (1965).

[20] J.H. Shim, K. Haule, G. Kotliar, Nature **446**, 513 (2007).

[21] O.K. Andersen, Phys. Rev. B **12**, 3060 (1975); M.S.S. Brooks and J.P. Kelly, Phys. Rev. Lett. **51**, 1708 (1983).

[22] J.M. Wills and O. Eriksson, Phys. Rev. B **45**, 13879 (1992); O. Eriksson, P. Söderlind, and J.M. Wills, Phys. Rev B **45**, 12588 (1992).

[23] P. Söderlind, G. Kotliar, K. Haule, P.M. Oppeneer, and D. Guillaumont, MRS Bulletin **35**, 883 (2010).

[24] B. Johansson, Phys. Rev. B **11**, 2740 (1975).

[25] O. Eriksson, J.D. Becker, A.V. Balatsky, and J.M. Wills, J. Alloys Compd. **287**, 1 (1999); A. B. Schick and V. A. Gubanov, Europhys. Lett. 69, 588 (2005); X. Wu, A. K. Ray Phys. Rev. B **72**, 045115 (2005).

[26] S.Y. Savrasov and G. Kotliar, Phys. Rev. Lett. **84**, 3670 (2000).

[27] A. Georges, G. Kotliar, W. Krauth, and W. Rozenberg, Rev. Mod. Phys. **68**, 13 (1996).

[28] W. Xiong, W. Xie, C. Shen, D. Morgan, J. Nucl. Mater. **443**, 331 (2013).

[29] P. Söderlind, B. Sadigh, V. Lordi, A. Landa, P.E.A. Turchi, J. Nucl. Mater. **444**, 356 (2014).

[30] J. Perdew, J.A. Chevary, S.H. Vosko, K.A. Jackson, M.R. Pederson, and D. J. Singh, Phys. Rev. B **46**, 6671 (1992); J. Perdew, K. Burke, and M. Ernzerhof, Phys. Rev. Lett. **77**, 3865 (1996).

[31] P. Söderlind, O. Eriksson, B. Johansson, and J.M. Wills, Phys. Rev. B **50**, 7291 (1994); P. Söderlind and A. Gonis, Phys. Rev. B **82**, 033102 (2010).

[32] J. M. Wills, M. Alouani, P. Andersson, A. Delin, O. Eriksson, O. Grechnyev, "*Full-Potential Electronic Structure Method"* (Springer-Verlag, Berlin, Heidelberg 2010).

[33] A. Zunger, S.-H. Wei, L.G. Ferreiram, and J. E. Bernard, Phys. Rev. Lett. **65**, 353 (1990).

[34] L. Vitos, "*Computational Quantum mechanics for Materials Engineers: The EMTO Method and Applications"* (Springer-Verlag, London 2007).

[35] J. Kollar, L. Vitos, and H.L. Skriver, in: H. Dreyssé (Ed.), "*Electronic Structure and Physical Properties of Solids: The Uses of the LMTO Method"*, Lecture Notes in Physics (Springer-Verlag, Berlin, Heidelberg, New York, 2000), pp. 85-113.

[36] D.J. Chadi and M.L. Cohen, Phys. Rev. B **8**, 5747 (1973); S. Froyen, Phys. Rev. B **39**, 3168 (1989).

[37] L.V. Pourovskii, A.V. Ruban, L. Vitos, H. Ebert, B. Johansson, and I.A. Abrikosov, Phys. Rev. B 71, 094415 (2005).

[38] J. S. Faulkner, Prog. Mater. Sci. **27**, 1 (1982).

[39] L. Vitos, I.A. Abrikosov, and B. Johansson, Phys. Rev. Lett. **87**, 156401 (2001).

[40] A.V. Ruban and H. L. Skriver, Phys. Rev. B **66**, 024201 (2002).

[41] A.V. Ruban, S. I. Simak, P. A. Korzhavyi, and H. L. Skriver, Phys. Rev. B **66**, 024202 (2002).

[42] A.V. Ruban, S.I. Simak, S. Shallcross, and H.L. Skriver, Phys. Rev. B **67**, 214302 (2003).

[43] I.A. Abrikosov, S.I. Simak, B. Johansson, A.V. Ruban, and H. L. Skriver, Phys. Rev. B **56**, 9319 (1997).

[44] B.L. Györffy, A.J. Pindor, G.M. Stocks, J. Staunton, and H. Winter, J. Phys. F: Met. Phys. **15**, 1337 (1985).

[45] P. Söderlind, A. Landa, and B. Sadigh, Phys. Rev. B **66**, 205109 (2002).

[46] A. Landa, P. Söderlind, and A.V. Ruban, J. Phys.: Condens. Matter **15**, L371 (2003).

[47] F.D. Murnaghan, Proc. Natl. Acad. Sci. U.S.A. **30**, 244 (1944).

[48] O. Gunnarson, O. Jepsen, and O.K. Andersen, Phys. Rev B **27**, 7144 (1983).

[49] I.A. Abrikosov and H.L. Skriver, Phys. Rev B **47**, 16532 (1993).

[50] A.V. Ruban and H.L. Skriver, Comput. Mater. Sci. **15**, 119 (1999).

[51] N.E. Christensen and S. Satpathy, Phys. Rev. Lett. **55**, 600 (1985).

[52] A.P. Miodownik, "*Phenomenological calculations of phase equilibria: the CALPHAD approach*", in NATO-ASI Proceedings, Series B: Physics, Vol. **319**, eds. P.E.A. Turchi and A. Gonis (Plenum Press, NY, 1994), p. 45-79.

[53] Hans Leo Lucas, Suzana G. Fries, and Bo Sundman, "*Computational Thermodynamics – The Calphad Method*" (Cambridge University Press, Cambridge, 2007).

[54] A. Dinsdale, CALPHAD **15**, 317-425 (1991).

[55] O. Redlich and A. Kister, Ind. Eng. Chem. **40**, 345-348 (1948).

[56] Y.M. Muggianu, M. Gambino, and J.P. Bros, J. Chem. Phys. **22**, 83-88 (1975).

[57] The Thermo-Calc and DICTRA applications software are products of Thermo-Calc AB; B. Sundman, B. Jansson, and J.-O. Andersson, "The Thermo-Calc Databank System", CALPHAD **9** (4), 153 (1985); J.-O. Andersson, T. Helander, L. Höglund, Pingfang Shi, and B. Sundman, "THERMO-CALC & DICTRA, computational tools for materials science", CALPHAD **26** (2), 273-312 (2002); cf. also http://www.thermocalc.se.

[58] A. Engström, L. Höglund, and J. Ågren, Metall. Mater. Trans. **25A**, 1127-1134 (1994); A. Borgenstam, A. Engström, L. Höglund, and J. Ågren, J. of Phase Equil. **21** (3), 269-280 (2000).

[59] A. Landa, P. Söderlind, and P.E.A. Turchi, J. Alloys Compd. **478**, 103 (2009).

[60] A. Landa, P. Söderlind, P.E.A. Turchi, L. Vitos, and A. Ruban, J. Nucl. Mater. **385**, 68 (2009).

[61] M. Kurata, T. Ogata, K. Nakamura, and T. Ogawa, J. Alloys Comp. **271/273**, 636 (1998).

[62] M. Kurata, CALPHAD **23**, 305-317 (1999).

[63] A. Landa, P. Söderlind, and P.E.A. Turchi, J. Nucl. Mater. **414**, 132 (2011).

[64] A. Landa, P. Söderlind, and P.E.A. Turchi, J. Nucl. Mater. **434**, 31 (2013).

[65] X. Zhang, Y. F. Cui, G. L. Xu, W. J. Zhu, H. S. Liu, B. Y. Yin, and Z. P. Jin, J. Nucl.

Mater. **402**, 15 (2010).

[66] S. Bajaj, A. Garay, A. Landa, P. Söderlind, P. Turchi, and R. Arróyave, J. Nucl. Mater. **409**, 1 (2011).

[67] A. Landa, P. Söderlind, P.E.A. Turchi, L. Vitos, and A. Ruban, J. Nucl. Mater. **393**, 141 (2009).

[68] A. Landa, P. Söderlind, B. Grabowski, P.E.A. Turchi, A. Ruban, and L. Vitos, in: D. Andersson, T. Durakewicz, C.H Booth, M. Stan, P.C. Burns, V. Tikare, R. Caciuffo, S.-W. Yu, R. Devanathan (Eds.), Actinides and Nuclear Energy Materials, Material Research Society, vol. 1444 (Cambridge University Press, Cambridge, 2012), pp. 67-78.

[69] A. Landa, P. Söderlind, P.E.A. Turchi, L. Vitos, O.E. Peil, and A.V. Ruban, J. Nucl. Mater. **408**, 61 (2011).

[70] P.E.A. Turchi, A.I. Landa, and P.A. Söderlind, J. Nucl. Mater. **418**, 165 (2011).

[71] A.A. Bochvar, S.T. Konobeevsky, V.I. Kutaitsev, T.S. Menshikova, and N.T. Chebotarev, "Interaction of Plutonium and other metals in connection with their arrangement in Mendeleev's periodic table", Proceedings of the Second United Nations International Conference on the Peaceful Uses of Atomic Energy, Geneva, 1958, Vol. 6, p. 184-193, United Nations, Geneva (1958).

[72] F.W. Schonfeld, E.M. Cramer, W.N. Miner, F.H. Ellinger, and A.S. Coffinberry, Prog. Nucl. Energy, Ser. **5**, Vol.**2**, 579, 599 (1959).

[73] J.J. English, "Molybdenum-Plutonium System, Binary and Ternary Phase Diagrams of Cb, Mo, Ta, and W", DMIC Rep., p 47 (1961).

[74] P.G. Mardon, J.P. Evans, D.J. Hodkin, and J.M. North, "The constitution and fabrication of Uranium-Molybdenum-Plutonium fuels", in Plutonium 1960: The Proceedings of the 2nd International Conference on Plutonium Metallurgy, ed. by E. Gibson, B.H. William, and D. Robert (Cleaver-Hume Press, London, 1961), pp. 329-352.

[75] F.H. Ellinger, W.N. Miner, D.R. O'Boyle, and F.W. Schonfeld, "Constitution of Plutonium Alloys", Los Alamos Scientific Laboratory Report LA-3870, 63-64 (December 1968).

[76] D.F. Bowersox and J.A. Leary, J. of Nucl. Mater. **27**, 181-186 (1968).

[77] L. Brewer, R.H. Lamoreaux, R. Ferro, R. Marazza, and K. Girgis, At. En. Rev. Special Issue No. 7, Ed. by L. Brewer (IAEA, Vienna, 1980).

[78] F.H. Ellinger, K.A. Johnson, and V.O. Struebing, J. of Nucl. Mater. **20**, 83 (1966).

[79] V.D. Shushakov, N.S. Kosulin, and N.T. Chebotarev, Problems of Nuclear Science and Engineering, Series Materials Science and New Materials (**3**) (1990) 14.

[80] A.G. Seleznev, N.S. Kosulin, and V.D. Shushakov, Phys. Met. Metall. **44**, 180 (1978).

[81] A.G. Seleznev, V.D. Shushakov, and N.S. Kosulin, Phys. Met. Metall. **46**, 193 (1979).

[82] P.E.A. Turchi and A.I. Landa, "Thermodynamic Database – Lower Length Scale, Part I: Thermodynamic Assessment of the Ternary Alloy System Mo-Pu-U", LLNL Technical Report LLNL-TR-553775 (April 26, 2012).

[83] A. Berche, N. Dupin, C. Guéneau, C. Rado, B. Sundman, and J.C. Dumas, J. of Nucl. Mater. **411**, 131-143 (2011).

[84] E. Perez, A. Ewh, J. Liu, B. Yuan, D.D. Keiser Jr., Y.H. Sohn, J. of Nucl. Mater. **394**, 160-165 (2009).

[85] P.E.A. Turchi and A.I. Landa, "Thermodynamic Database – Lower Length Scale, Part II: Thermodynamic Assessment of Al-Mo-Si-U", LLNL Technical Report LLNL-TR-603054 (September 26, 2012).

[86] V. Lordi and P.E.A. Turchi, unpublished (2013).

[87] C. Audet, G. Savard and W. Zghal, "Multiobjective optimization through a series of single-objective formulations", SIAM J. Opt. **19** (1), 188-210 (2008); and references therein.

[88] A.M. Savchenko, A.V. Vatulin, A.V. Morozov, G.V. Kulakov, S.A. Ershov, A.V. Laushkin, S.V. Maranchak, Y.V. Konovalov, and E.K. Malamanova, "Zirconium alloys matrix as innovative material for composite fuel", Prog. in Nucl. Energy **57**, 138-144 (2012).

[89] R.D. Mariani, D.L. Porter, S.L. Hayes, and J. Rory Kennedy, Private Communication (2012).